



Quasi-static and dynamic Brazilian testing and failure analysis of a deer antler in the transverse to the osteon growth direction

Can Tuncer^a, Mustafa Güden^b, Mehmet Orhan^{a,*}, Mustafa Kemal Sarıkaya^b, Alper Taşdemirci^b

^a Department of Mechanical Engineering, Faculty of Engineering, Pamukkale University, Denizli, Turkey

^b Department of Mechanical Engineering, Faculty of Engineering, İzmir Institute of Technology, Urla, İzmir, Turkey

ARTICLE INFO

Keywords:

Deer antler
Split Hopkinson pressure bar
Anisotropy
Mechanics

ABSTRACT

The transverse tensile strength of a naturally fallen red deer antler (*Cervus Elaphus*) was determined through indirect Brazilian tests using dry disc-shape specimens at quasi-static and high strain rates. Dynamic Brazilian tests were performed in a compression Split-Hopkinson Pressure Bar. Quasi-static tensile and indirect Brazilian tests were also performed along the osteon growth direction for comparison. The quasi-static transverse tensile strength ranged 31.5–44.5 MPa. The strength increased to 83 MPa on the average in the dynamic Brazilian tests, proving a rate sensitive transverse strength. The quasi-static tensile strength in the osteon growth direction was however found comparably higher, 192 MPa. A Weibull analysis indicated a higher tensile ductility in the osteon growth direction than in the transverse to the osteon growth direction. The microscopic analysis of the quasi-static Brazilian test specimens (tensile strain along the osteon growth direction) revealed a micro-cracking mechanism operating by the crack deflection/twisting at the lacunae in the concentric lamellae region and at the interface between concentric lamellae and interstitial lamellae. On the other side, the specimens in the transverse direction fractured in a more brittle manner by the separation/delamination of the concentric lamellae and pulling of the interstitial lamellae. The detected increase in the transverse strength in the high strain rate tests was further ascribed to the pull and fracture of the visco-plastic collagen fibers in the interstitial lamellae. This was also confirmed microscopically; the dynamically tested specimens exhibited flatter fracture surfaces.

1. Introduction

The deer antler is a bony protrusion and often used in the fights between male deer with a goal of gaining a territory and priority in breeding. The fighting causes serious injuries, even fatalities, and the success is largely determined by the strength of antler (Clutton-Brock et al., 1979; Johnson et al., 2007). The architectural structure and mechanical properties of the deer antlers have been taken considerable scientific interest (Cappelli et al., 2015; Hellmich et al., 2004; Landete-Castillejos et al., 2013; Zioupos et al., 1996). The cross-section of the deer antler comprises an interior cancellous or spongy bone and an outer compact or cortical bone as shown in Fig. 1. The basic structure of the compact bone is made of osteons, ~100 μm in size, (Fig. 1). The osteons accommodate vertical and horizontal canals, sequentially called the Haversian and Volkmann canals, for the circulation of blood and nutrition. Each osteon is made of concentric lamellae in several micron thickness. Each concentric lamella is made of collagen fibers (in several micron diameter), which is composed of collagen fibrils, 200–300 nm,

and the carbonated hydroxyapatite crystals (Fig. 1) (Chen et al., 2009a). The lamellae in between the osteons are called the interstitial laminae. The mineralized collagen fibers inside the lamellae surround the osteons helically, forming the basic structure of the cylindrical horn (Olszta et al., 2007; Rolf and Enderle, 1999; Weiner and Wagner, 1998). The collagen fibers in concentric lamellae are oriented differently, leading to high resistance to torsional loads. The osteons are presumably oriented in the bone growth direction. The anisotropy, mineral deposition, orientation of osteons, size of existing pores, and connection among the pores are also effective on the mechanical strength (Gibson et al., 1997; Reilly and Burstein, 1975; Currey, 1975; Bonfield and Clark, 1973).

Previous studies on the mechanical response of bone mostly focused on the anisotropy in the quasi-static mechanical behavior of tissue in anatomical regions of complex biological systems, examples of which can be found in refs. (Dendorfer et al., 2008; Wolfram et al., 2010; Aiyangar et al., 2014; Goda and Ganghoffer, 2015). Fang et al. (2018) applied quasi-static three-point bending tests in the longitudinal, transverse, and radial directions of deer antler specimens. A relatively

* Corresponding author.

E-mail address: morhan@pau.edu.tr (M. Orhan).

<https://doi.org/10.1016/j.jmbbm.2023.105648>

Received 31 May 2022; Accepted 1 January 2023

Available online 4 January 2023

1751-6161/© 2023 Elsevier Ltd. All rights reserved.

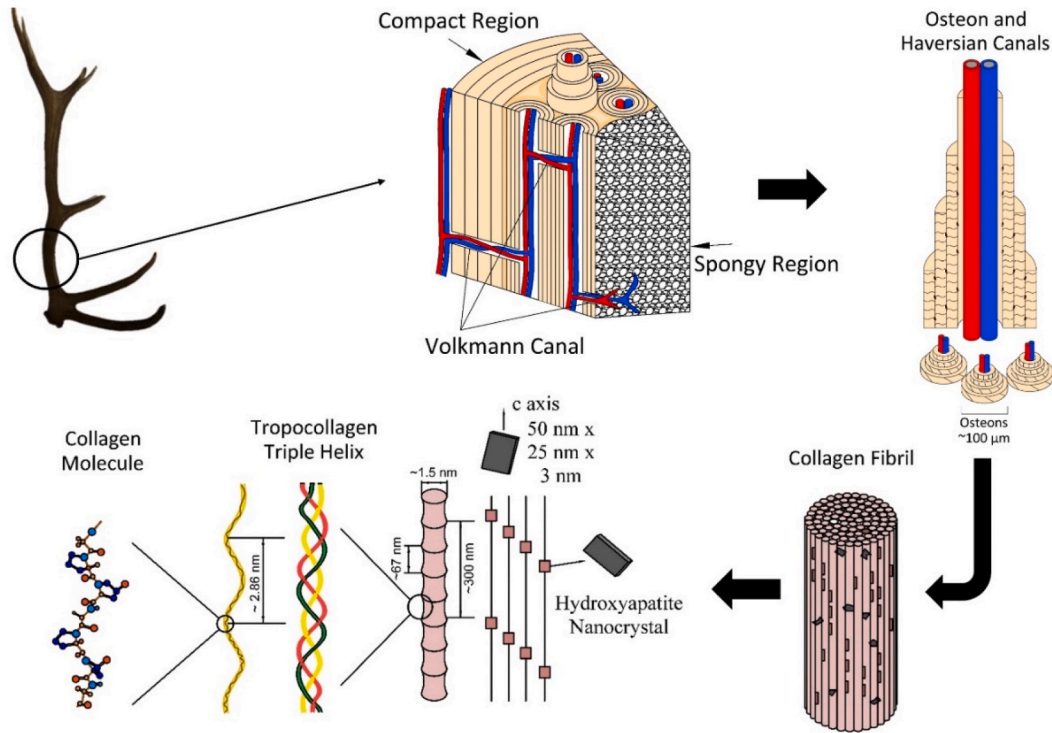


Fig. 1. The schematic of the hierarchical structure of the deer antler (Chen et al., 2009b).

high bending strength was reported for the transverse direction (268.6 MPa), while the strengths were shown similar in the longitudinal (47.73 MPa) and radial (42.71 MPa) directions. Adharapurapu et al. (2006) tested dry and wet bovine cortical bones through parallel and perpendicular to the growth axis (longitudinal and transverse directions) in the strain rate range 10^{-3} - 10^3 s⁻¹. High strain rate tests were conducted in a compression Split Hopkinson Pressure Bar (SHPB). The results showed a higher strength in the longitudinal axis than in the transverse one; a higher bone durability in the dry than in the wet condition, and an increased strength at increasing strain rates at the expense of the reduced fracture strain. Bekker et al. (2015) tested the bovine cortical bone in both longitudinal and transverse directions at the quasi-static

strain rates between 10^{-4} and 10^{-1} s⁻¹ and high strain rates between 2.5×10^2 and 10^3 s⁻¹. The compressive strength varied between 149.6 MPa and 234.8 MPa at the quasi-static strain rates; however, it increased to 383.9 MPa at 2.5×10^2 s⁻¹ and 413.9 MPa at 10^3 s⁻¹. Ferreira et al. (2006) reported 240 ± 66.4 MPa for the high strain rate compressive strength of a bovine cortical bone in the transverse direction and 281 ± 42.4 MPa in the longitudinal direction. A higher elastic modulus in the longitudinal direction (9.9 ± 2.7 GPa) than in the transverse direction (6.8 ± 2.1 GPa) was also reported in the same study. Kulin et al. (2011) tested 6 months to 28 years old horse cortical bones at 10^{-3} , 1 and 10^3 s⁻¹. The longitudinal compressive strengths were reported 180, 350 and 500 MPa and the transverse compressive strengths 120, 200 and 320

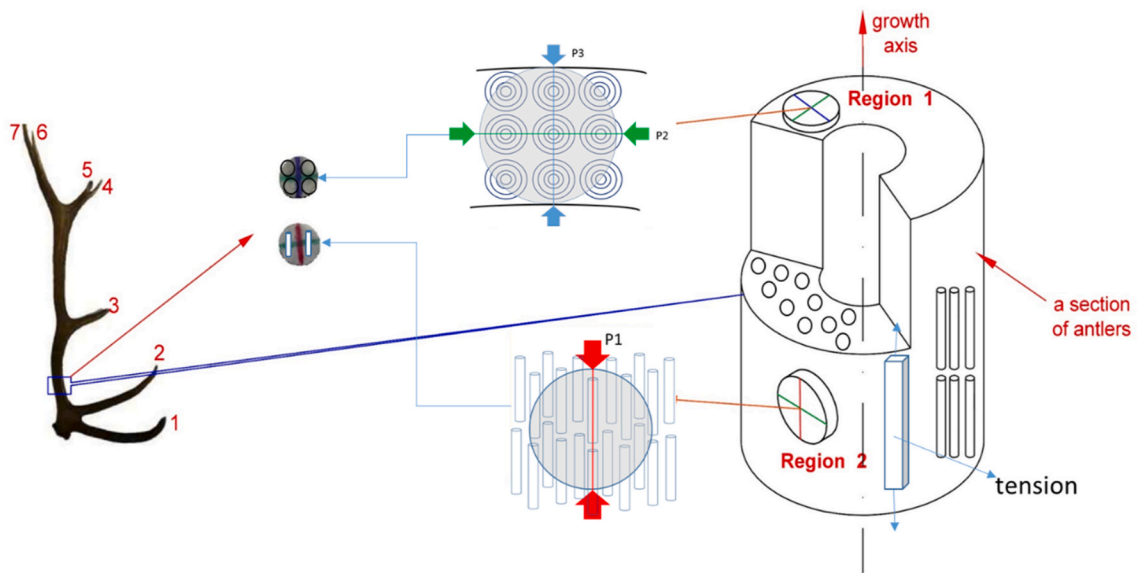


Fig. 2. The location the cut-section (for specimen preparation) on the as-received antler and test specimen directions: P₁ longitudinal direction, P₂ transverse direction and P₃ radial direction.

MPa at 10^{-3} , 1 and 10^3 s^{-1} , respectively. Shunmugasamy et al. (2010) tested the epiphyses and diaphyses regions of the rabbit femur at quasi-static and high strain rates. Although, the Diaphyses test specimens showed lower strengths (42.0–56.3 MPa) than the epiphyses specimens (92.4–103.9 MPa) at quasi-static strain rates, they showed higher strengths (187.0–242.8 MPa) than the epiphyses specimens (82.4–100.6 MPa) at high strain rates between 274 and 722 s^{-1} . In another study, Pilcher et al. (2010) investigated the elastic modulus of bovine tibia. A micro-CT technique was used to identify the direction of fibers and to exclude voids in trabecular region. The modulus of elasticity was also computed from configurational details extracted from micro-CT images between 10^{-3} and 500 s^{-1} . The modulus of elasticity was shown to increase with increasing strain rate.

Since the cortical bone thickness of the deer antlers is relatively small, 4–5 mm, the use of conventional test methods in order to extract the material mechanical property data for the transverse tensile strength is rather difficult as they require mostly larger specimen sizes. Therefore, Brazilian tests were employed to small size, disc-shape deer cortical bone specimens in order to determine the transverse tensile strength, the interlayer strength of osteon-matrix interface of a deer antler at a quasi-static and a high strain rate. Brazilian test was first developed by Carneiro (1943) and Akazawa (A, 1943) in 1943 and has become a common method to determine the tensile strength of brittle materials including concrete, rock and ceramics. It is also a good candidate to investigate the biomechanical behavior of the cortical layers of the archaeological bones (Turner-Walker and Parry, 1995) and the artificially aged bones (Turner-Walker, 2011).

2. Materials, testing and characterization

A naturally fallen red deer antler, the so-called Cervus Elaphus from the Çivril-Akdağ forestry district of Denizli in Turkey was used to prepare test specimens in present study. A section near the bottom of the as-received antler was cut as shown schematically in Fig. 2. The thickness of the compact bone region in the cut-section varied between 1.5 and 4 mm. The discs were initially drawn on the surface of the cut-section with the red, blue and green lines on them in order to identify the directions during the tests, as shown in Fig. 2. The disc-shape specimens were extracted through the radial, transverse, and longitudinal directions of the osteon growth axis using a diamond-tipped tubular drill bit and P120 grit sandpapers to fit final size as suggested by ASTM D3967-95a standard (ASTMD3967-95a, 2001). In Fig. 2, the red line represents the parallel, the green line perpendicular (transverse), and the blue line radial to the growth axis. In the same figure, P_1 refers to the test in the longitudinal direction, P_2 in the transverse direction and P_3 in the radial direction. Furthermore, a special care was taken during specimen preparation in order to ensure that the test specimens contained no spongy bone. Total 40 test specimens were prepared for the quasi-static and 12 for the high strain rate tests. According to ASTM D3967 - 95a, the thickness/diameter ratio of the test specimen should be between 0.2 and 0.75. Therefore, for the quasi-static test specimens, the diameter varied between 7.75 and 8 mm and the thickness between 3 and 3.15 mm while keeping the thickness/diameter ratio at 0.4. The specimens for the SHPB tests had a thickness to diameter ratio of ~ 0.3 with a diameter of ~ 9.75 mm and a thickness of 3 mm. The final sizes of the specimens and their directions on the antler are shown in Fig. 2. In addition to Brazilian tests, direct tensile tests were applied to the longitudinal direction (Fig. 2) in order to observe the mechanical contribution of osteons on overall strength. Test specimens of the direct tensile test were 65 mm length, 7 mm width, and 3 mm in thickness. All test specimens were dried in an oven at 60°C for 60 min before testing.

The tensile stress, σ_t , of a disc specimen in Brazilian test is given as (ASTM, 2017)

$$\sigma_t = \frac{2P}{\pi t D} \quad (1)$$

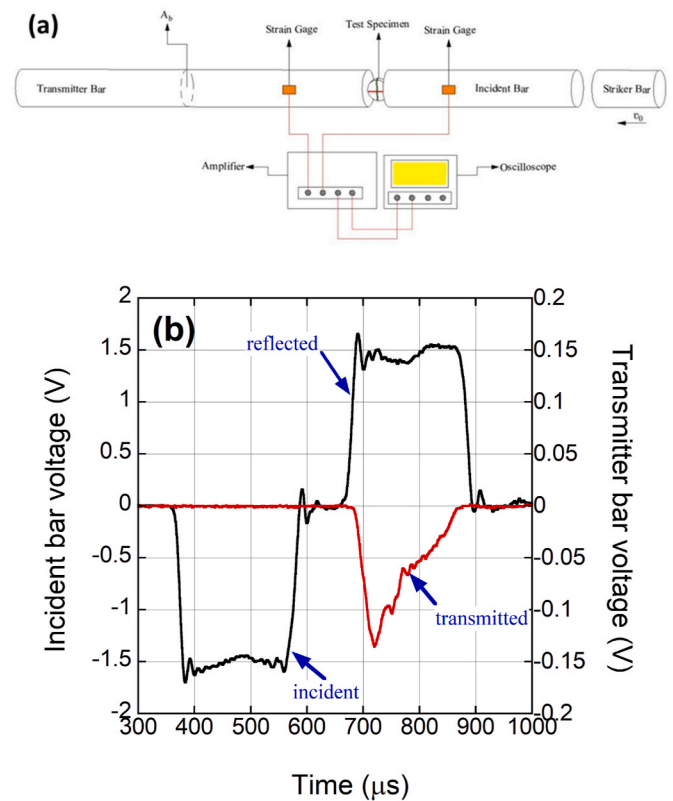


Fig. 3. (a) schematic representation of the Dynamic Brazilian SHPB set-up and (b) a typical voltage reading of the SHPB.

Here, P is the applied load and t and D are the thickness and diameter of the test specimen, respectively. The quasi-static tests were performed in a Shimadzu AG-X conventional test device at displacement rates 0.05 mm s^{-1} and 0.02 mm s^{-1} for Brazilian test and tensile tests. Dynamic Brazilian tests were performed in an Inconel 718 bar compression SHPB set-up. As schematically shown in Fig. 3(a), the test specimens were inserted in between the incident and transmitter bars having both the diameters of 19.40 mm and the lengths of 2000 and 1800 mm, respectively. An incoming incident wave was induced on the incident bar by the impact of a 50 mm-long Inconel striker bar having the same diameter as the incident bar. A full Wheatstone-bridge of 350Ω foil strain gages captured the incident, reflected and transmitted strains on the bars; then the strains were recorded by means of an oscilloscope and amplifier. Based on the one-dimensional elastic stress wave propagation in long bars (Kolsky, 1949; Davies and Hunter, 1963), the displacement (d_s), indirect tensile stress (σ_{st}) and displacement rate (\dot{d}_s) of specimen were determined using the following relations

$$d_s(t) = -2C_b \int_0^t \varepsilon_R(t) dt \quad (2)$$

$$\sigma_{st}(t) = \frac{2A_b E_b \varepsilon_T(t)}{\pi t D} \quad (3)$$

$$\dot{d}_s(t) = -2C_b \varepsilon_R(t) \quad (4)$$

In above relations, A_b , A_s , E_b , C_b and t are sequentially the bar cross-sectional area, the specimen cross-sectional area, the bar elastic modulus, the bar elastic wave velocity and the time and ε_R and ε_T are the reflected and transmitted strains, respectively. A high speed camera, Photron Fastcam SA1.1, captured the deformation of specimens during the tests at 100,000 fps. A typical voltage reading of the SHPB Brazilian test is shown in Fig. 3(b). The maximum in the transmitter bar voltage

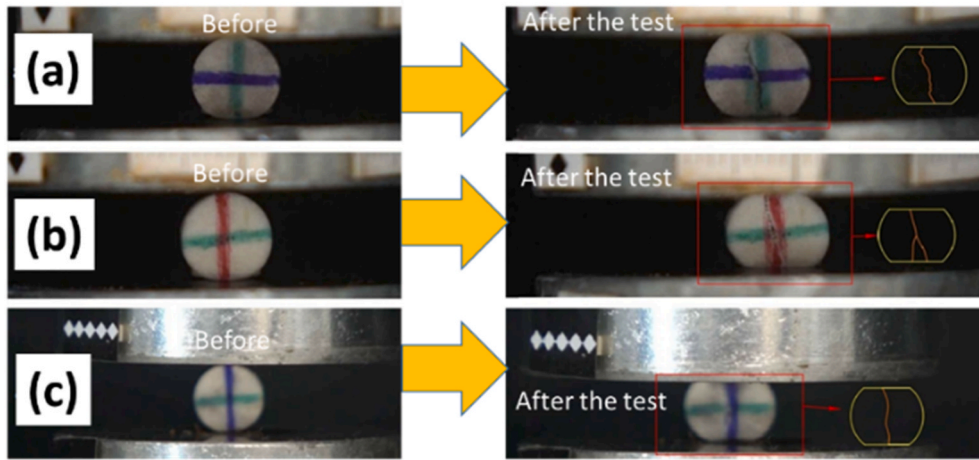


Fig. 4. The pictures of Brazilian test specimens before and after test (a) transverse, (b) longitudinal and (c) radial direction.

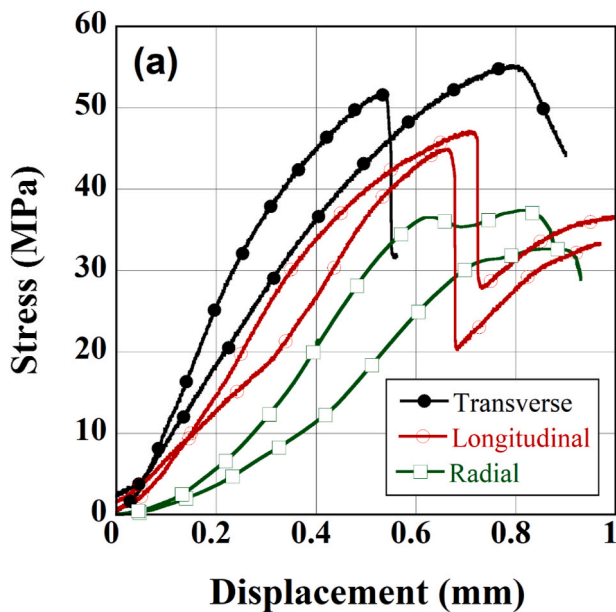


Fig. 5. Representative stress-displacement curves of Brazilian transverse, radial and longitudinal directions.

(negative) corresponds to the maximum stress in the specimen, while a linear loading behavior is notable before the maximum. Stress equilibrium in the SHPB is important for the validity of the test results (Ravichandran and Subhash, 1994) and this was checked and proved by comparing the forces on the incident and transmitter bars. The specimens extracted parallel to the growth axis (longitudinal direction) failed by forming a single tensile crack on the loading axis, while the specimens loaded in the transverse directions formed a global deformation/crushing in the SHPB. Hence, the dynamic stress-displacement curves of the specimens parallel to the growth axis were reported, while the dynamically crushed transverse axis specimens were examined microstructurally in the SEM in order to reveal the micro-mechanisms leading to global crushing. Finally, the microscopic analyses of the deformed and fractured specimens were performed in a ZEISS-SUPRA 40 VP FESEM SEM. Before imaging, samples were coated with Gold/Palladium (80%/20%) using Quorum Q150R ES brand device.

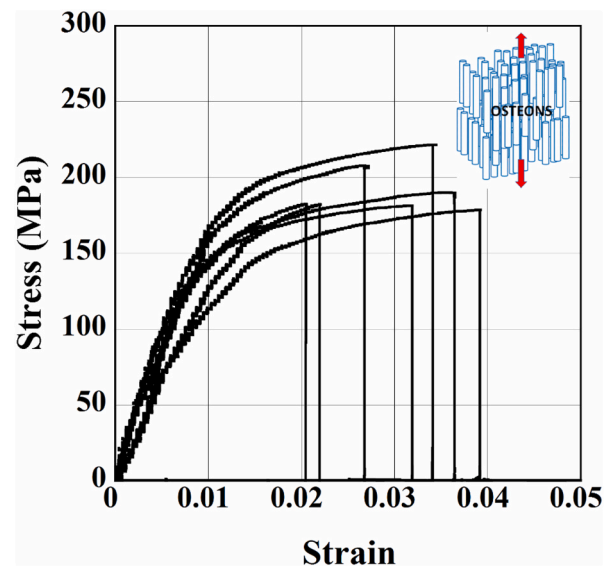


Fig. 6. Engineering stress-strain tension curves in the longitudinal direction (osteon growth direction).

3. Results and discussion

3.1. Indirect and direct tensile tests

Fig. 4(a–c) show the pictures of the valid test Brazilian test specimens before and after the test for transverse, longitudinal and radial directions. As is seen for each direction, a center line crack forms along the marked direction, showing the development of a tension failure due to transverse tensile strain/stress. The representative quasi-static stress-displacement curves of loading in transverse, radial and longitudinal directions are shown in Fig. 5. The tensile strength is almost the same for the transverse and longitudinal directions, sequentially 44.5 and 43.8 MPa on the average (at least 7 tests were performed for each direction). However, the tensile strength is relatively lower, 31.5 MPa, for loading in the radial direction.

The stress-strain curves of 7 tensile specimens in the osteon growth direction are shown in Fig. 6. The stress-strain curves show a substantial deformation after the elastic region, confirming an elastic-plastic behavior of the tensile tested antler specimens in the longitudinal direction. The average tensile strength, failure strain and elastic modulus

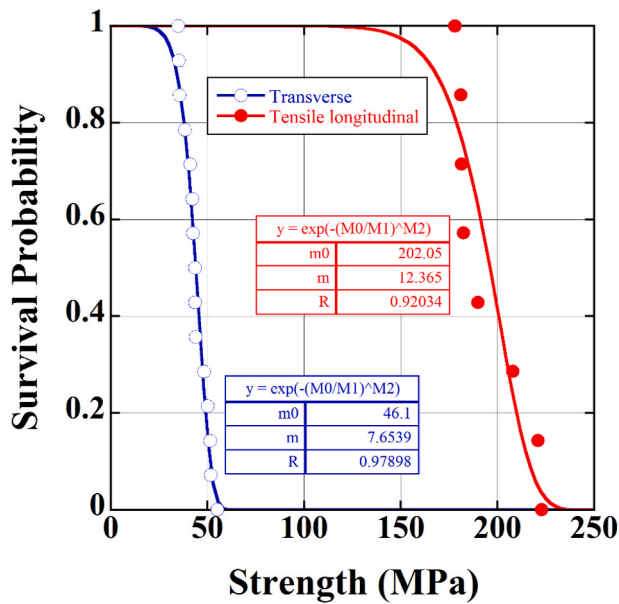


Fig. 7. The Weibull survival probability $P(V)$ vs strength for transverse and longitudinal direction.

are sequentially ~192 MPa, 0.03 and 18.45 GPa. The measured average mechanical properties are found very much comparable with the previous studies considering the variations of the mechanical properties between different species and ages of deer. For example, the tensile strength and strain and elastic modulus were reported 158 MPa, 0.11 and 7.2 GPa for a red deer (Currey, 1998) and 188 MPa, 0.0146 and 17.11 GPa for a spotted deer (RAJARAM and RAMANATHAN, 1982) in dry condition. In another study, the tensile and transverse strength of an elk antler were reported 115 and 20.3 MPa, respectively (Chen et al., 2009b).

The fracture strength of the tested samples was fitted with the Weibull distribution (Weibull, 1951). The Weibull survival probability $P(V)_s$ is

$$P(V)_s = \exp \left[- \left(\frac{\sigma}{\sigma_0} \right)^m \right] \tag{6}$$

where m is the Weibull modulus, σ is the stress and σ_0 is the characteristic stress. The Weibull modulus represents how rapidly the strength falls as the stress approaches σ_0 . The method shows a distribution, when $\sigma = 0$ then $P(V)_s = 1$ and $\sigma = \sigma_0$ then $P(V)_s = 0.37$. In general, the m parameter varies between 1 and 15 for brittle materials. The Weibull modulus and the characteristic stress values of transverse and longitudinal direction strengths are shown in Fig. 7. The m value is 12.3 and 7.6 for the longitudinal and transverse directions and the transverse direction is therefore more brittle than the longitudinal direction based on the calculated m values. The m values were previously reported higher for longitudinal (6.4) than the transverse direction (3.1) for an elk antler (Chen et al., 2009b). Although higher m values found in the present study, the m value of longitudinal direction is almost two times that of transverse, similar to the m values given in ref. (Chen et al., 2009b). The difference in m values between longitudinal and transverse directions are related with the fracture mechanism operative in both directions, which will be elaborated later.

The stress-displacement and displacement rate-displacement curves of 4-SHPB tests subjected to loading in the transverse direction are shown in Fig. 8(a). In the same figure, a typical quasi-static curve is also shown for comparison. Note that the tests in Fig. 8(a) were performed using the same gas gun pressure; hence, the incident waves were almost the same for each, while the variations seen in the stresses were due to the variations in the microstructures between the tested specimens.

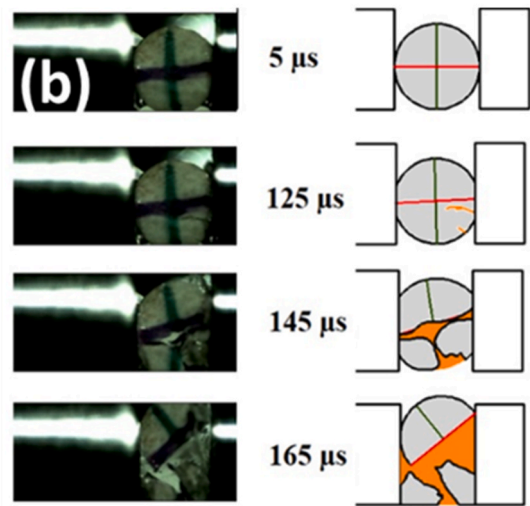
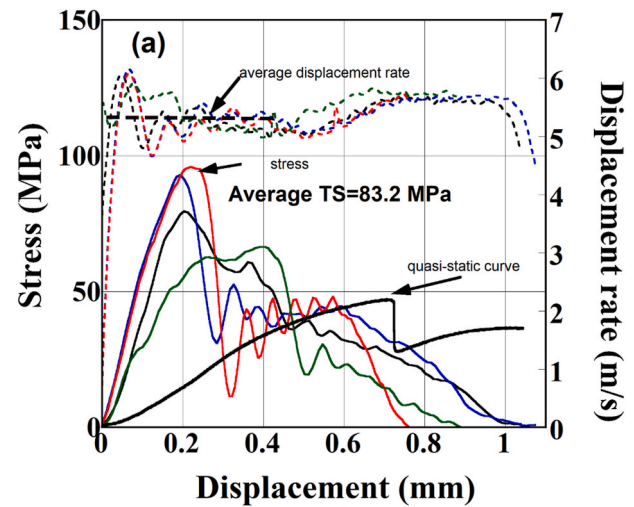


Fig. 8. (a) SHPB stress-displacement and displacement rate-displacement curves (four tests) in the longitudinal direction of the antler and (b) deformation pictures of a SHPB specimen at different times.

Anyway, the stresses and displacement rates are seen to be comparable and the maximum stress varies between 66 and 96 MPa with an average of 83.2 MPa and the displacement rates are around 5.2 m/s as shown in Fig. 8(a). Note also that the transverse tensile strength increases significantly at the dynamic loading rates, by about 40 MPa on the average as compared with that of quasi-static loading rate, proving a rate sensitive tensile strength in the transverse direction with respect to the osteon growth axis. On the other side, the displacements corresponding to the tensile strength almost reduces to the half of quasi-static rate as seen in Fig. 8(a). The pictures of a SHPB specimen at different deformation times are shown in Fig. 8(b). The axial cracking in this test started at about 40 μ s; hence, the specimen rotation occurred later, after the crack initiation. A similar specimen rotation is also noted at quasi-static rates.

3.2. Microscopic observations

In order to see development of microcracks within the osteons and interstitial bone, indirect compression tests were performed on the longitudinal specimens (specimens obtained from region 2) in a direction normal to the osteon growth direction. These samples showed no fracture but slightly compressed/crushed through their diameters. Fig. 9 (a) and (b) show the SEM micrographs of one of these samples normal

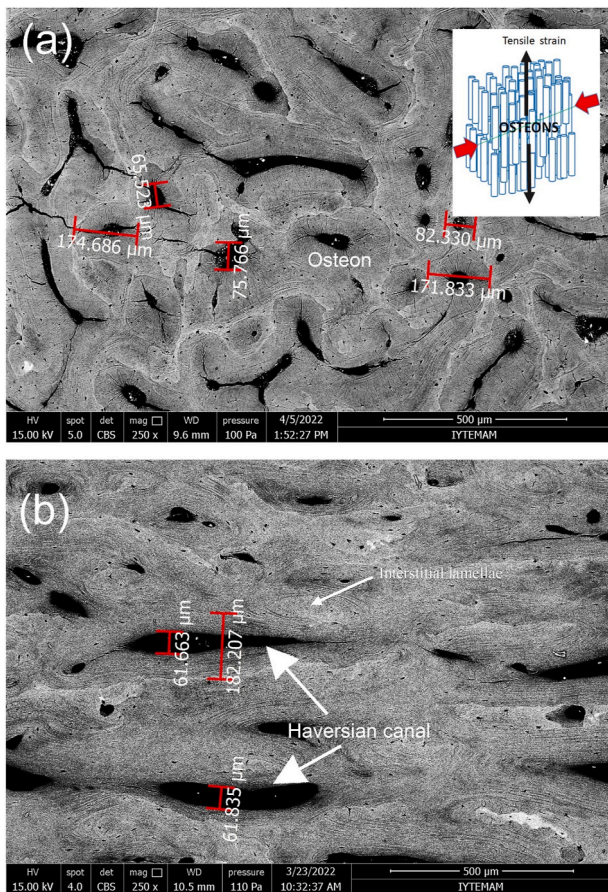


Fig. 9. SEM micrographs shown the cross-sections of the longitudinal specimens quasi-statically compressed in a direction normal to the osteon growth direction, (a) normal and (b) along to osteon growth direction.

and along the osteon direction, respectively. The induced transverse tensile strain (indirect test) is therefore parallel to the osteon growth direction. In the inset of Fig. 9(a), the osteon growth direction and the loading direction (red arrows) are also shown. In the transverse directions, the osteons and Haversian canals are clearly seen. The micro-cracks around the Haversian canals inside the osteons are formed due to the applied indirect tensile strain in the osteon direction. Haversian and

Volkman canals promote micro cracking within the osseous structure. Some of big micro-cracks initiate on the tip of the Haversian although fine ones were directed to surface normal of the Haversian canal. Propagation of such micro-cracks evolve across the barrier created by lamellae of osteons. Therefore, the route of micro-cracks is determined by the inorganic matrix occupying the space among the type I collagen fibrils. Furthermore, smaller Haversian canals were vulnerable to stresses leading to considerable number density of micro-cracks along the whole surface of them. Crack bridging was also observed along the splayed Haversian canals irrespective to the distance between the tips of neighbors as seen in Fig. 9(a). In contrast to osteons, interstitial lamellae having no Haversian canal do not contain any micro-cracks. The diameter of few osteons and Haversian canals are measured as shown in the same micrograph. Small osteons have the sizes of 82 μm and the largest ones 175 μm. The sizes of Haversian canals are 65–75 μm. These numbers are also confirmed by the measurement made along the longitudinal direction as seen in Fig. 9(b). The measured diameter of Haversian canals is about 61 μm and the size of one osteon is 182 μm as seen in the same figure. The osteons are surrounded by a cement line (interstitial lamellae or interstitial bone), which is seen whiter in Fig. 9 (a) with a thickness of several tens of microns. Above observations were also made previously (Launey et al., 2010; Pazzaglia et al., 2012; Dhari et al., 2021). The sizes of osteons and Haversian canals are anticipated to vary with age and species.

The SEM micrographs of the fracture surfaces of transversely (a specimen of region 1) and longitudinally (a specimen of region 2) loaded Brazilian test specimens are shown in Fig. 10(a) and (b). The loading directions (LD) in both specimens are shown by the arrow in Fig. 10(a), and the specimen thicknesses are also marked in the same figures. Note that the indirect tensile strain is normal to the fracture surface in both specimens: Haversian canals are clearly seen on the fracture surfaces of both specimens: along the thickness in the transverse specimen (Fig. 10 (a)) and along the loading direction in the longitudinal specimen (Fig. 10(b)). In both loadings, Haversian canals play the major role in global failure (see black arrow representing two halves of the same Haversian canal, in fact two halves of an osteon, in Fig. 10(a)). As discussed previously, lamellae of osteons delaminate at the inorganic matrix, mostly hydroxyapatite crystals whose dimension is of the few nanometers. The appearances of both Haversian and Volkmann's canals on the fracture surfaces are tended to conclude that these canals are acting as voids in the dry condition, impairing the transverse tensile strength.

The SEM micrographs of the fracture surface of a quasi-static transverse Brazilian test specimen (specimen of region 1) are shown in Fig. 11

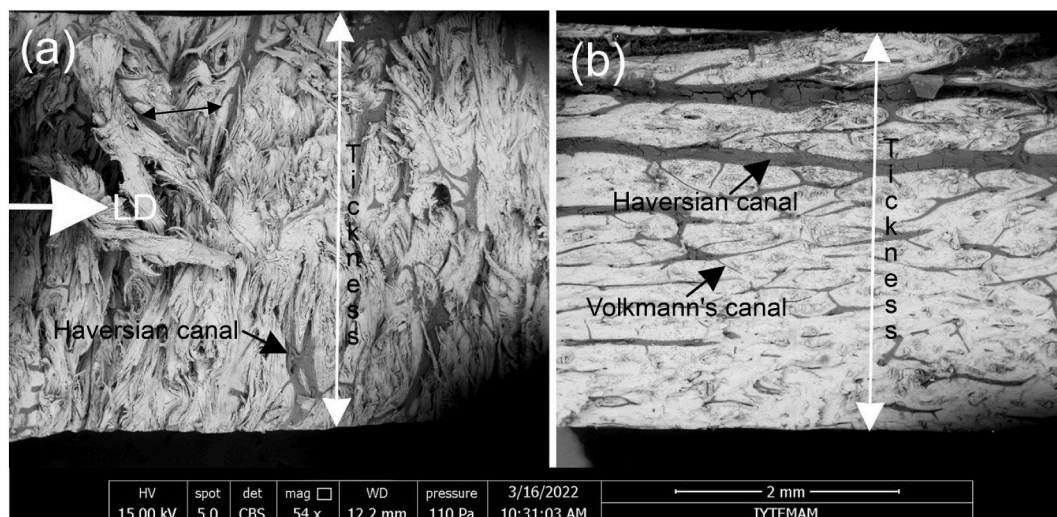


Fig. 10. SEM micrographs showing the fracture surfaces of quasi-static (a) transverse and (b) longitudinal the quasi-static Brazilian test specimens.

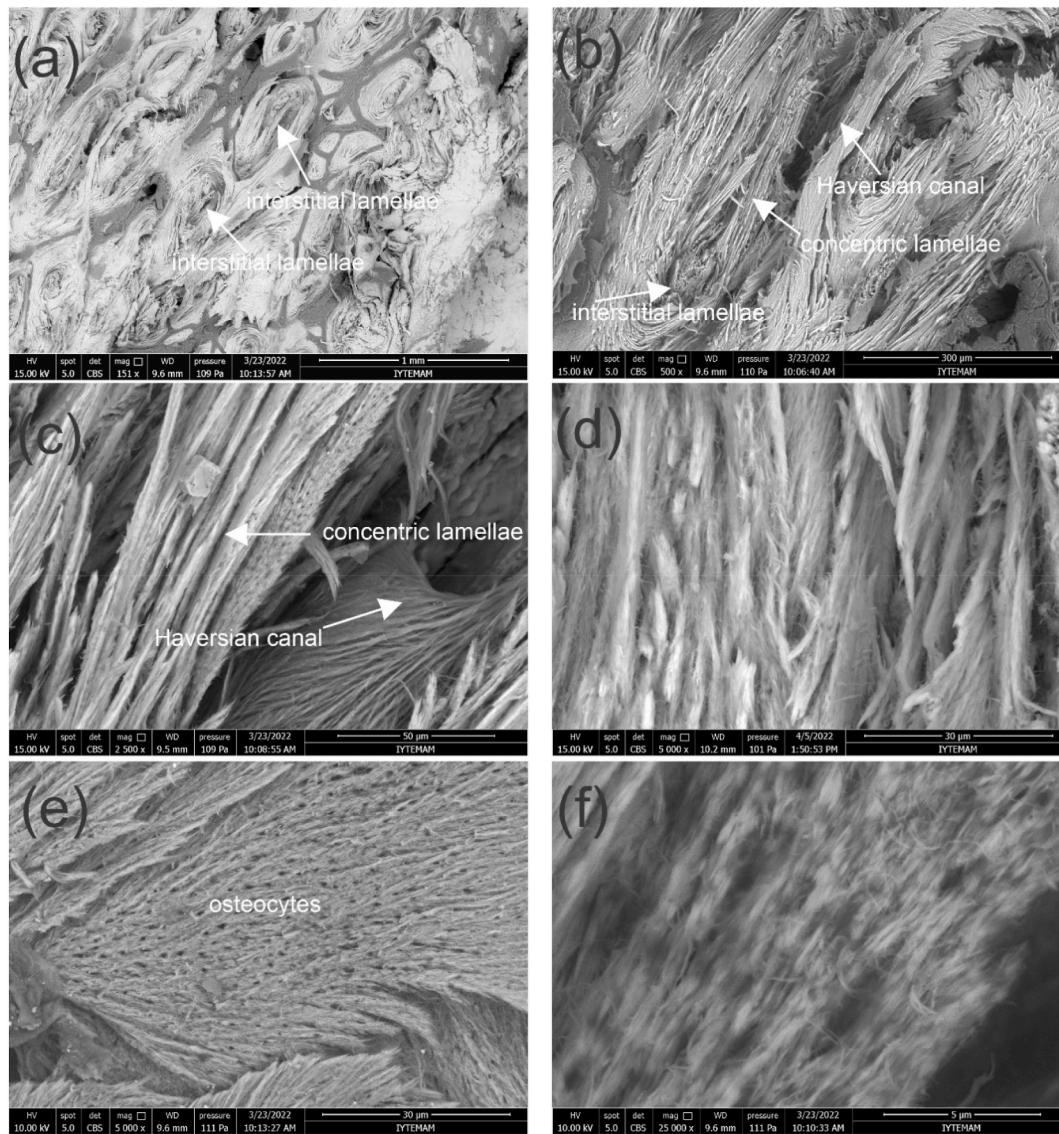


Fig. 11. SEM micrographs showing the fracture surfaces of a quasi-static transverse specimen a) concentric and interstitial lamellae at a (a) smaller and (b) larger magnification, (c) concentric lamellae, (d) magnified concentric lamellae in (c) showing collagen fibers and fibrils, (e) delaminated concentric lamellae showing osteocytes and (f) magnified concentric lamellae in (e).

(a–f). The delaminated/separated concentric lamellae around Haversian canals and the pulled and separated/fractured interstitial lamellae in between the concentric lamellae are clearly seen in Fig. 11(a) and (b). The separation occurs within a lamella, while delamination between lamellae. A close inspection of concentric lamellae region clearly indicates both the delaminated and separated concentric laminates in Fig. 11(c). The separated concentric lamellae is composed of collagen fibers (few microns) and fibrils (few nanometers) as depicted in Fig. 11(d). On the surface of a delaminated lamellae shown in Fig. 11(e), osteocytes are clearly seen. The osteocytes are located in between concentric lamellae. At a higher magnification, the orientation of the collagen fibrils is seen in Fig. 11(f). In the transverse direction, the failure mode in the concentric lamellae region is the separation of collagen fibers in each lamella and delamination of lamellae. While the failure mode in the interstitial lamellae region is the pulling and separation (fracture) of collagen fibers as will be elaborated below.

The SEM micrographs of the fracture surface of a quasi-static longitudinal Brazilian test specimen are shown in Fig. 12(a–f). Again, the delaminated/separated concentric lamellae around Haversian canals and the pulled and separated/fractured interstitial lamellae in between

the concentric lamellae are seen in Fig. 12(a) and (b). The separation between concentric and interstitial lamellae regions is more apparent in Fig. 12(c), in which the collagen fibers in the concentric lamellae region are seen normal to the indirect tensile strain (Fig. 12(d)), while the collagen fibers in the interstitial lamellae region are seen parallel to the indirect tensile strain (Fig. 12(e)). The collagen fibers in the interstitial lamellae region are pulled in the indirect tensile strain direction. These two different collagen fiber orientations lead to a change crack path on the fracture surface in between two regions. Fig. 12(f) shows a region from the fracture surface between concentric and interstitial lamellae regions. The arrows in the same figure show the change of crack path between these two regions.

Fig. 13(a–f) show the fracture surface of a dynamically loaded specimen in the longitudinal direction (specimen obtained from region 2). As seen in Fig. 13(a–e), Haversian canals laying out along the longitudinal direction of osteons create voids whereas calcified tissue is subjected pulling out perpendicular to fractured surface. This delamination is clearly visible at the interface of two concentric lamellae forming a whole osteon (Fig. 13(a)). On the other hand, in Fig. 13(b), the osteon appears to be completely separated in the mineralized region

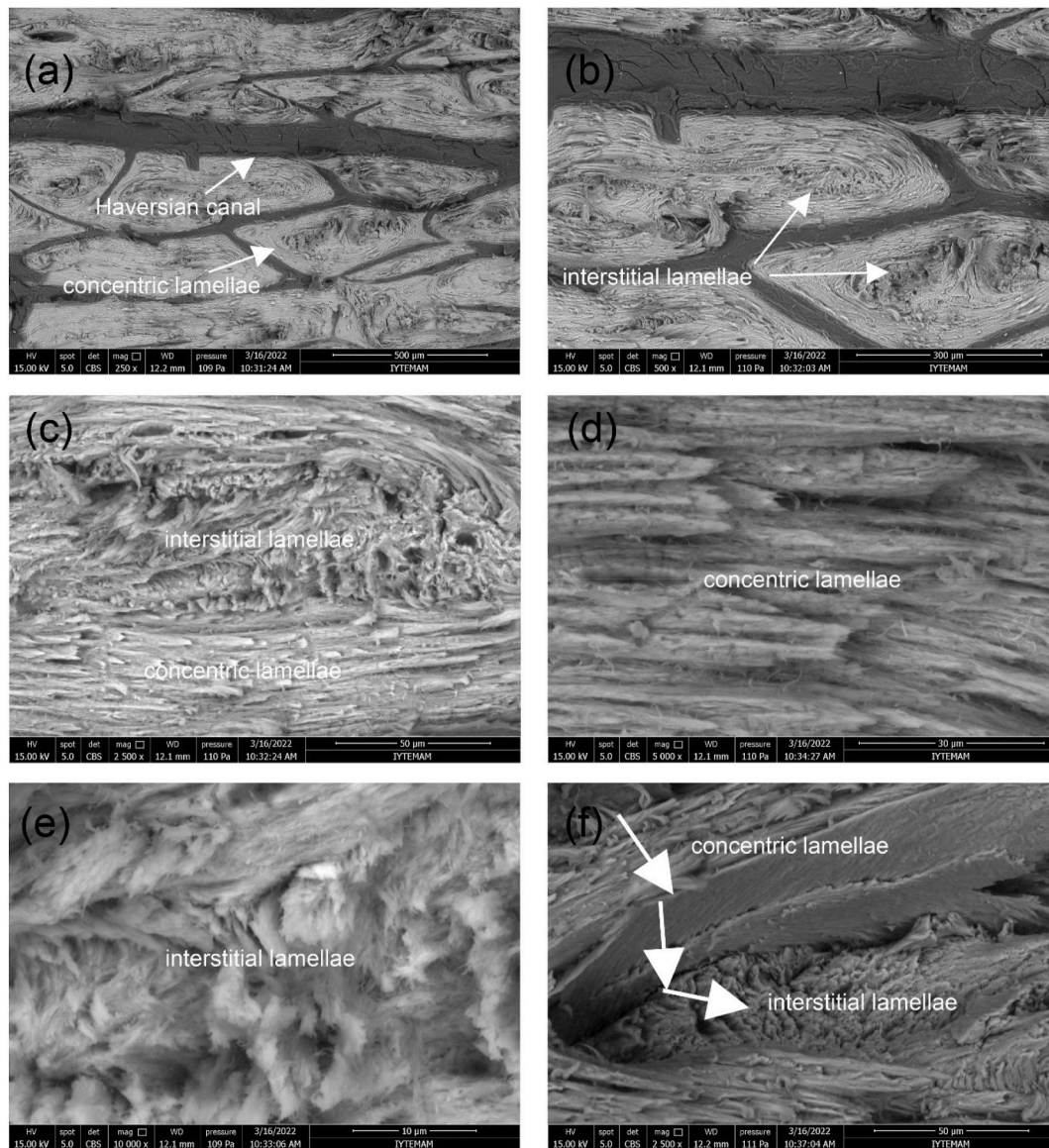


Fig. 12. SEM micrographs showing the fracture surfaces of a quasi-static longitudinal specimen a) concentric and interstitial lamellae at a (a) smaller and (b) medium and (c) larger magnification, (d) magnified concentric lamellae in (c) showing collagen fibers and fibrils, (e) magnified interstitial lamellae in (c) showing broken fiber and fibrils, (f) a fracture region between concentric and interstitial lamellae showing the change of failure mechanism between concentric and interstitial lamellae regions.

where concentric osteons are attached to each other due to the tensile stresses. In Fig. 13(c–e), it is observed that the cross-linking fibers that develop perpendicular to the osteons break apart as well as the concentric lamellae fibers that are separated from each other. The contribution of cross-linking fibers to mechanical strength, of course, depends on their number density in the structure. Fig. 13(f) shows lacunae hosting osteocytes.

Fig. 14(a and b) show the SEM micrographs of the polished cross-section of an indirect compression longitudinal test specimen (a specimen of region 2) in a direction normal to the osteon growth axis. The tensile strain was indirectly formed along the osteon growth axis and the pictures were taken normal to the osteons. These tests give an indirect analysis of the tensile failure in the osteon growth axis. Microcracks are seen in Fig. 14(a) as marked by the arrows in each osteon, which tends to conclude that the cracks are initially initiated in the concentric lamellae region through micro-cracking. A close inspection of each osteon reveals the formation of multiple of radial and small, and large size cracks (Fig. 14(a) and (b)). Majority of these cracks are arrested and deflected

by different mechanisms as marked in Fig. 15(a and b). The crack bridging occurs by (a) lacuna crack bridging (LCB) and (b) interface (between concentric and interstitial lamellae) crack bridging and crack deflection/twisting occur by the lacuna crack bridging and deflection (LCBD): interface crack deflection (ICD) and by interface crack twisting (ICT). The crack path is bridged and also twisted (90° at the interface) in the interstitial lamellae region. The microcracks forms in the concentric lamellae region is in fact separation of collagen fibers/lamellae delamination as seen in Fig. 16(a–d).

The main deformation mechanisms under tensile loading in the longitudinal direction are therefore micro caking of the concentric lamellae, leading to major crack into the interstitial lamellae region (Fig. 14(a) and (b)). The cracks propagation is further enhanced in the interstitial lamellae region by the transverse and twisted crack paths and even micro-cracking occurs in this region as depicted in Fig. 14(b). The highest toughness detected in the longitudinal direction of elk antler was reported due to micro-scale toughening mechanisms such as in-plane crack deflection and out-of plane crack (Koester et al., 2008; Krauss

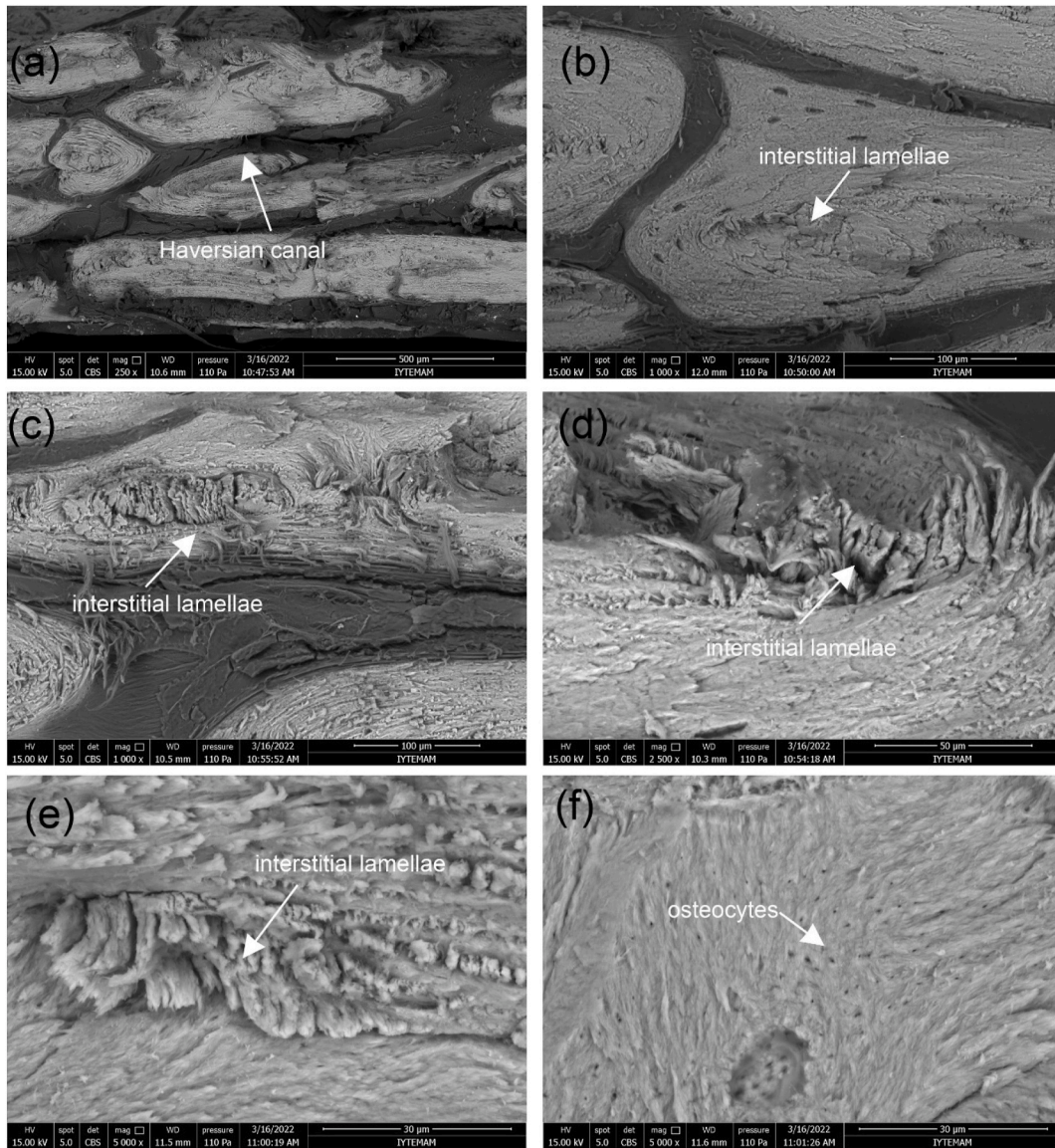


Fig. 13. SEM micrographs showing the fracture surfaces of a dynamically loaded longitudinal specimen's concentric and interstitial lamellae at a (a) smaller and (b) medium and (c) larger magnification, (d) and (e) magnified interstitial lamellae region and (f) delaminated concentric lamellae showing osteocytes.

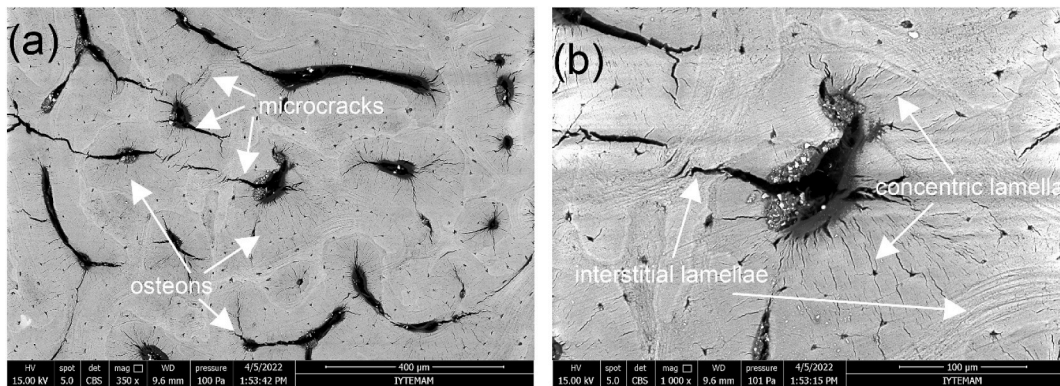


Fig. 14. (a–b) SEM micrographs of the polished cross-section of an indirect compression test longitudinal specimen in a direction normal to the osteon growth direction (not fractured); the tensile strain indirectly formed along the osteons and the pictures were taken normal to the osteons.

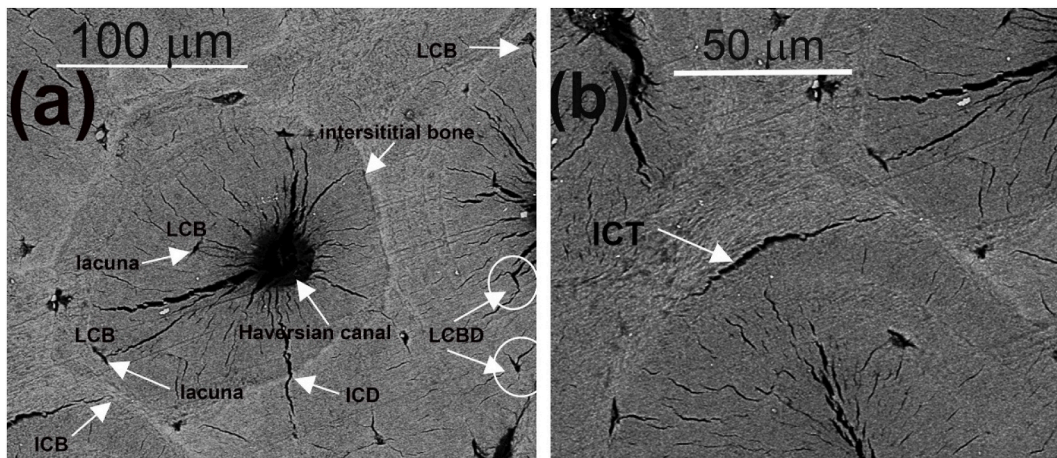


Fig. 15. (a–b) SEM micrographs of the polished cross-section of an indirect compression test longitudinal specimen in a direction normal to the osteon growth direction (not fractured); the tensile strain indirectly formed along the osteons and the pictures were taken normal to the osteons. (a) LCB: lacuna crack bridging, LCBBD: lacuna crack bridging and deflection and ICD: interface crack deflection and ICB: interface crack bridging and (b) ICT: interface crack twisting.

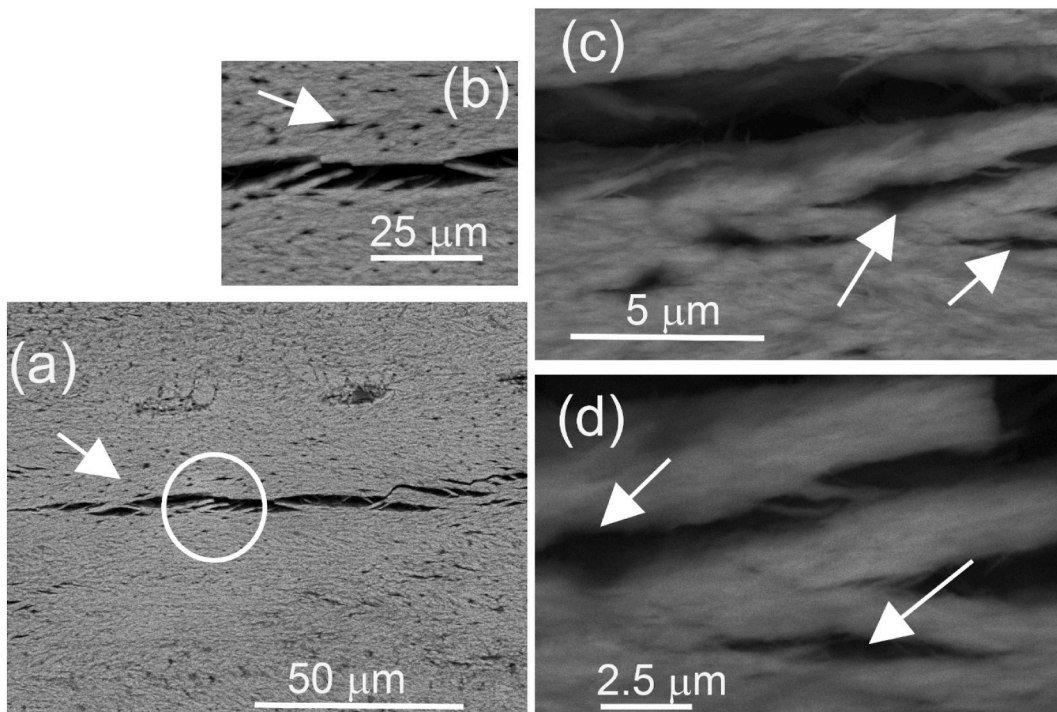


Fig. 16. (a–d) SEM micrographs of the polished cross-section of an indirect compression test longitudinal specimen in a direction normal to the osteon growth direction (not fractured); the tensile strain indirectly formed along the osteons and the pictures were taken normal to the osteons. a-d showing the delamination of concentric lamellae through the lacunae (osteocytes).

et al., 2009; Gupta et al., 2013). Here, it was proposed that the canaliculi, microscopic canals between the lacunae, provided an easy micro-cracking side which contributed to the observed visco-plastic behavior of the antler in the osteon growth axis.

Active osteoblasts are located at the periphery of bone matrix and secrete type I collagen proteoglycans, and matricellular glycoproteins. Each osteoblast is bounded by integrins. When osteoblast activity is completed, each osteoblast is entrapped by the matrix secreted and differentiates as osteocytes hosted by lacuna. During the differentiation from the osteoblast to osteocyte, the cell within the lacuna takes a long dendritic form so called canaliculi enclosed by calcified matrix. Fluid induced shear stresses within canaliculi and mechanical strain through perilacunar matrix are two theories trying to reveal osteocyte processes

(Prendergast and Huiskes, 1996; Walker et al., 2000; Nicoletta et al., 2006; Robling and Bonewald, 2020). Furthermore, geometry and mechanical behavior of actin network seems to be responsible for resisting stresses generated by pericellular space around the osteocytes (You et al., 2004). In the context of this study, we believe that potential mechanism lying behind the twisting, deflection and restraining of micro-cracks by lacunae and accompanying dendritic canals is strictly based upon material on the perilacunar bone matrix and shear thickening actin filaments in response to high strain rates (Norstrom and Gardel, 2011).

Fig. 17(a) shows a partially lamination of a dynamically crushed sample. The formation of a few interfaces of lamination (Fig. 17(e) perpendicular to the direction of loading can be easily observed on the

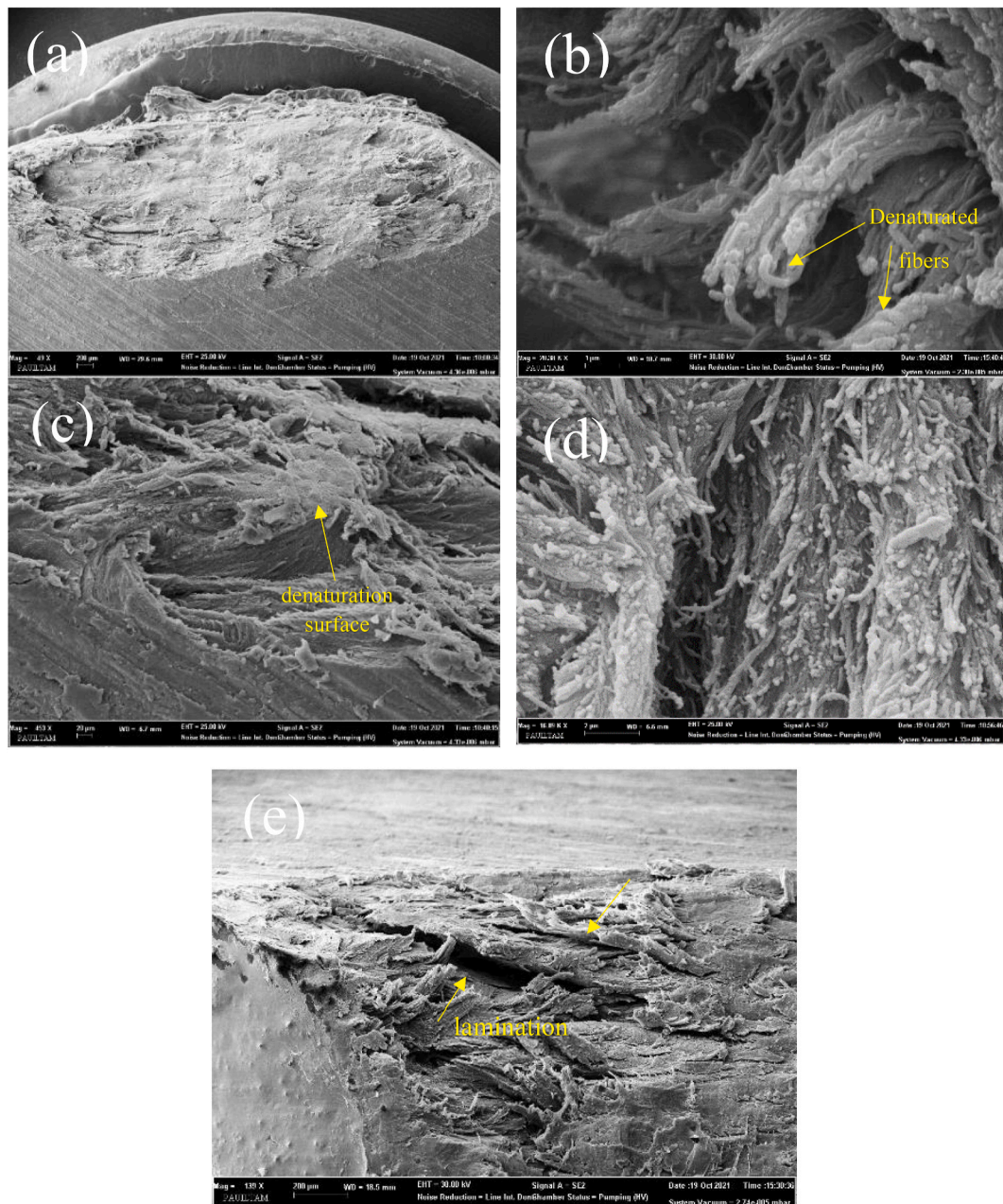


Fig. 17. View of a globally crushed specimen subjected to dynamical loading in transverse direction (a) whole specimen (b) a cluster of denatured collagen fibers at 1 μm (c) a denaturated surface (d) Denaturated collagen fibers lying on the surface of a main osteon fiber (e) regions where lamination occur.

damaged surface. It is obvious that porous specimen is heated non-uniformly due to mechanical work leading to high pressures. Therefore, it is not at all unlikely that the stress can reach much higher values in transverse loading compared to longitudinal one. Therefore, there will be drastic increase of temperature in microscopic regions where large pressure variations exit with respect to very small time increments. Denaturation as consequence of heating/pressurization of collagen fibrils is a phenomenon that greatly reduces the mechanical strength of the structure and disrupts its structural integrity (Wang et al., 2002; Marques et al., 2003; Potekhin et al., 2009; Suwa et al., 2015; Lucila-Lambri et al., 2018). In a temperatures range, 80° - 190° or at pressure around 320 MPa, partial or complete denaturation weakens adhesion between the collagen particles and destabilizes collagen structure of the tissue. It is presumed that collagen fibers denatured and lost their stability during the loading leads to surface fragmentation.

4. Conclusions

The transverse tensile strength of a naturally fallen red deer's antler, the so-called Cervus Elaphus, (from the Çivril-Akdağ forestry district of Denizli in Turkey) was determined through indirect Brazilian tests using disc-shaped dry samples in three different directions with respect to osteon growth axis. High strain rate tests were performed in a compression SHPB to reveal any strain rate effect on the transverse tensile strength. Quasi-static tensile tests were also performed along the osteon growth direction for a comparison between average transverse and longitudinal strength values. The quasi-static transverse tensile strength in each direction varied between 31.5 and 44.5 MPa. The transverse tensile strength increased to 83 MPa on the average in the dynamic Brazilian tests, proving a rate sensitive transverse tensile strength of the tested antler. The tensile strength in the osteon growth axis was found comparable higher, 192 MPa. Weibull analysis indicated

a higher tensile ductility in the osteon growth axis as compared with the transverse axis. A microscopic analysis on the Brazilian test specimens in which a tensile strain formed along the osteon growth axis revealed a micro-cracking mechanism operating by crack deflection/twisting at the lacunae in the concentric lamellae region and at the interface between concentric lamellae and interstitial lamellae. On the other side, the specimens were fracture in the transverse direction in a more brittle manner by the separation/delamination of the concentric lamellae and pulling of interstitial lamellae. The detected increased transverse strength in the high strain rate tests was ascribed to the pull and fracture of the visco-plastic collagen fiber in the interstitial lamellae. This was further confirmed by an observation of the more brittle appearance of the dynamically tested specimen's fracture surface under microscope.

CRedit authorship contribution statement

Can Tuncer: Data curation, Formal analysis, Investigation, Validation, Visualization. **Mustafa Güden:** Conceptualization, Data curation, Formal analysis, Supervision, Writing – original draft, Writing – review & editing. **Mehmet Orhan:** Resources, Supervision, Writing – review & editing, Funding acquisition, Investigation, Methodology. **Mustafa Kemal Sarıkaya:** Data curation, Formal analysis. **Alper Taşdemirci:** Methodology.

Declaration of competing interest

The authors declare that they have no known competing financial interests or personal relationships that could have appeared to influence the work reported in this paper.

Acknowledgement

This study was supported by The Council of Higher Education (YOK) 100/2000, Scientific and Technological Research Council of Turkey (TUBITAK) 2211/A Scholarship Program, and Unit of Scientific Research Projects (USRP) of Pamukkale University. The grant number is 2020FEBE035. The numerical calculations reported in this paper were partially performed at TUBITAK ULAKBIM, High Performance and Grid Computing Center (TRUBA resources).

References

- A, T., 1943. A New Test Method for Evaluating Internal Stress Due to Compression of Concrete: the Splitting Tension Test, vol. 19. Japan Society of Civil Engineers, pp. 777–787.
- Adharapurapu, R., Jiang, F., Vecchio, K., 2006. Dynamic fracture of bovine bone. *Mater. Sci. Eng. C* 26, 1325–1332.
- Aiyangar, A., et al., 2014. Dependence of anisotropy of human lumbar vertebral trabecular bone on quantitative computed tomography-based apparent density. *J. Biomech. Eng.* 136 (9), 1–10.
- ASTM, 2017. *C496/C496M – 11 Standard Test Method for Splitting Tensile Strength of Cylindrical Concrete Specimens*.
- Astm3967-95a, 2001. Standard Test Method for Splitting Tensile Strength of Intact Rock Core Specimens. ASTM International.
- Bekker, A., et al., 2015. Constant strain rate compression of bovine cortical bone on the Split-Hopkinson Pressure Bar. *Mater. Sci. Eng. C* 46, 443–449.
- Bonfield, W., Clark, E.A., 1973. Elastic deformation of compact bone. *J. Mater. Sci.* 8, 1590–1594.
- Cappelli, J., et al., 2015. Manganese supplementation in deer under balanced diet increases impact energy and contents in minerals of antler bone tissue. *PLoS One* 10 (7), e0132738.
- Carneiro, F.L.L.B., 1943. A new method to determine the tensile strength of concrete. In: *Proceedings of the 5th Meeting of the Brazilian Association for Technical Rules*.
- Chen, P.-Y., Stokes, A.G., McKittrick, J., 2009a. Comparison of the structure and mechanical properties of bovine femur bone and antler of the North American elk (*Cervus elaphus canadensis*). *Acta Biomater.* 5 (2), 693–706.
- Chen, P.Y., Stokes, A.G., McKittrick, J., 2009b. Comparison of the structure and mechanical properties of bovine femur bone and antler of the North American elk (*Cervus elaphus canadensis*). *Acta Biomater.* 5 (2), 693–706.
- Clutton-Brock, T.H., et al., 1979. The logical stag: adaptive aspects of fighting in red deer (*Cervus elaphus L.*). *Anim. Behav.* 27, 211–225.
- Currey, J.D., 1975. The effects of strain rate, reconstruction and mineral content on some mechanical properties of bovine bone. *J. Biomech.* 8 (1), 81–86.

- Currey, J.D., 1998. Mechanical properties of vertebrate hard tissues. *Proc. IME H J. Eng. Med.* 212, 399–411.
- Davies, E.D.H., Hunter, S.C., 1963. The dynamic compression testing of solids by the method of the split Hopkinson pressure bar. *J. Mech. Phys. Solid.* 11 (3), 155–179.
- Dendorfer, S., et al., 2008. Anisotropy of the fatigue behaviour of cancellous bone. *J. Biomech.* 41 (3).
- Dhari, R.S., et al., 2021. Numerical investigation of Fibonacci series based bio-inspired laminates under impact loading. *Compos. Struct.* 255, 112985.
- Fang, Z., et al., 2018. Investigation of inner mechanism of anisotropic mechanical property of antler bone. *J. Mech. Behav. Biomed. Mater.* 88, 1–10.
- Ferreira, F., Vaz, M.A., Simões, J.A., 2006. Mechanical properties of bovine cortical bone at high strain rate. *Mater. Char.* 57 (2), 71–79.
- Gibson, L.J., Ashby, M.F., 1997. In: *Series, a.S.S.S. (Ed.), Cellular Solids: Structure and Properties*, 2 ed. Cambridge University Press.
- Goda, I., Ganghoffer, J.-F., 2015. Identification of couple-stress moduli of vertebral trabecular bone based on the 3D internal architectures. *J. Mech. Behav. Biomed. Mater.* 51, 1751–16161.
- Gupta, H.S., et al., 2013. Intrafibrillar plasticity through mineral/collagen sliding is the dominant mechanism for the extreme toughness of antler bone. *J. Mech. Behav. Biomed. Mater.* 28, 366–382.
- Hellmich, C., Barthelemy, J., Dormieux, L., 2004. Mineral-collagen interactions in elasticity of bone ultrastructure - a continuum micromechanics approach. *Eur. J. Mech. Solid.* 23 (5), 783–810.
- Johnson, H.E., et al., 2007. Effects of antler breakage on mating behavior in male tule elk (*Cervus elaphus nannodes*). *Eur. J. Wildl. Res.* 53 (1), 9–15.
- Koester, K.J., Ager, I., W, J., Ritchie, R.O., 2008. The true toughness of human cortical bone measured with realistically short cracks. *Nat. Mater.* 7 (8), 672–677.
- Kolsky, H., 1949. An investigation of the mechanical properties of materials at very high rates of loading. *Proc. Phys. Soc. B* 62 (11), 676.
- Krauss, S., et al., 2009. Inhomogeneous fibril stretching in antler starts after macroscopic yielding: indication for a nanoscale toughening mechanism. *Bone* 44 (6), 1105–1110.
- Kulin, R.M., J, F., Vecchio, K.S., 2011. Effects of age and loading rate on equine cortical bone failure. *J. Mech. Behav. Biomed. Mater.* 4 (1), 57–75.
- Landete-Castillejos, T., et al., 2013. Effects of public vs. private management on deer antler composition, mechanical and structural variables. *Eur. J. Wildl. Res.* 59 (4), 519–529.
- Launey, M.E., et al., 2010. Mechanistic aspects of the fracture toughness of elk antler bone. *Acta Biomater.* 6 (4), 1505–1514.
- Lucila Lambri, M., et al., 2018. Denaturation processes of collagen from cow bones as a function of temperature. *Materia-Rio De Janeiro* 23 (2).
- Marques, M.I., et al., 2003. Possible mechanism for cold denaturation of proteins at high pressure. *Phys. Rev. Lett.* 91 (13), 138103.
- Nicoletta, D.P., et al., 2006. Osteocyte lacunae tissue strain in cortical bone. *J. Biomech.* 39 (9), 1735–1743.
- Norstrom, M., Gardel, M.L., 2011. Shear thickening of F-actin networks crosslinked with non-muscle myosin IIB. *Soft Matter* 7 (7), 3228–3233.
- Olszta, M.J., et al., 2007. Bone structure and formation: a new perspective. *MATERIALS SCIENCE & ENGINEERING R-REPORTS* 58 (3–5), 77–116.
- Pazzaglia, U.E., et al., 2012. Morphometry and patterns of lamellar bone in human Haversian systems. *ANATOMICAL RECORD-ADVANCES IN INTEGRATIVE ANATOMY AND EVOLUTIONARY BIOLOGY* 295 (4), 1421–1429.
- Pilcher, A., et al., 2010. High strain rate testing of bovine trabecular bone. *Journal of Biomechanical Engineering* 132 (8), 1–7.
- Potekhin, S.A., et al., 2009. High pressure stabilization of collagen structure. *Biochimica et Biophysica Acta (BBA) - Proteins and Proteomics* 1794 (8), 1570–9639.
- Prendergast, P.J., Huiskes, R., 1996. Microdamage and osteocyte-lacuna strain in bone: a microstructural finite element analysis. *Journal of Biomechanical Engineering* 118 (2), 240–246.
- Rajaram, A., Ramanathan, N., 1982. Tensile properties of antler bone. *CALCIFIED TISSUE INTERNATIONAL* 34 (3), 301–305.
- Ravichandran, G., Subhash, G., 1994. CRITICAL-APPRAISAL of limiting strain rates for compression testing of ceramics in a split HOPKINSON pressure bar. *Journal of the American Ceramic Society* 77 (1), 263–267.
- Reilly, D.T., Burstein, A.H., 1975. The elastic and ultimate properties of compact bone tissue. *Journal of Biomechanics* 8 (6), 393–405.
- Robling, A.G., Bonewald, L.F., 2020. The osteocyte: new insights. *Annual Review of Physiology* 82, 485–506.
- Rolf, H.J., Enderle, A., 1999. Hard fallow deer antler: a living bone till antler casting? *The Anatomical Record* 255 (1), 69–77.
- Shunmugasamy, V.C., Gupta, N., Coelho, P.G., 2010. High strain rate response of rabbit femur bones. *Journal of Biomechanics* 43 (15), 3044–3050.
- Suwa, Y., et al., 2015. Thermal denaturation behavior of collagen fibrils in wet and dry environment. *Journal of Biomedical Materials Research Part B: Applied Biomaterials* 104 (3), 538–545.
- Turner-Walker, G., 2011. The mechanical properties of artificially aged bone: probing the nature of the collagen–mineral bond. *Palaeogeography, Palaeoclimatology, Palaeoecology* 310 (1), 17–22.
- Turner-Walker, G., Parry, T.V., 1995. The tensile strength of archaeological bone. *Journal of Archaeological Science* 22 (2), 185–191.
- Walker, L., et al., 2000. Calcium-channel activation and matrix protein upregulation in bone cells in response to mechanical strain. *JOURNAL OF CELLULAR BIOCHEMISTRY* 79 (4), 648–661.
- Wang, X., et al., 2002. Effects of collagen unwinding and cleavage on the mechanical integrity of the collagen network in bone. *Calcified Tissue International* 71 (2), 186–192.

- Weibull, W., 1951. A statistical distribution function of wide applicability. *Journal of applied mechanics* 18 (3), 293–297.
- Weiner, S., Wagner, H., 1998. The material bone: structure mechanical function relations. *ANNUAL REVIEW OF MATERIALS SCIENCE* 28, 271–298.
- Wolfram, U., Wilke, H.-J., Zysset, P.K., 2010. Rehydration of vertebral trabecular bone: influences on its anisotropy, its stiffness and the indentation work with a view to age, gender and vertebral level. *Bone* 46 (2), 348–354.
- You, L., et al., 2004. Ultrastructure of the osteocyte process and its pericellular matrix. *Anatomical Record Part A- Discoveries in Molecular Cellular and Evolutionary Biology* 278A (2), 505–513.
- Ziopoulos, P., Wang, X.T., Currey, J.D., 1996. Experimental and theoretical quantification of the development of damage in fatigue tests of bone and antler. *Journal of Biomechanics* 29 (8), 989–1002.